

ARTICLE OPEN

Electronic friction and tuning on atomically thin MoS₂Bin Shi¹, Xuehui Gan^{1,2}, Kang Yu¹, Haojie Lang¹, Xing'an Cao¹, Kun Zou¹ and Yitian Peng^{1,2}✉

Friction is an energy dissipation process. However, the electronic contribution to energy dissipation channels remains elusive during the sliding friction process. The friction and dissipation on atomically thin MoS₂ with semiconductive characteristics are studied and tuned by the gate-modulated carrier concentration. The electronic contribution to energy dissipation of friction on atomically thin MoS₂ was confirmed and regulated through tuning the strength of the electron-phonon coupling. The electron-phonon coupling can be strengthened and depressed to increase and decrease friction by the gate-modulation of the carrier concentration. The fitting of the friction on atomically thin MoS₂ and carrier concentration is approximately linear which is in accordance with Langevin equation induced friction. Then the active, dynamical, and repeated tuning of friction on atomically thin MoS₂ with semiconductive properties is achieved by the active modulation of carrier concentration with gate voltage. These observations help us to understand the electronic friction in essence, provide a utility approach to tune the friction intelligently on atomically thin two-dimensional materials with semiconductive properties and achieve superlubric properties for the application in various micro-and nanoelectromechanical systems.

npj 2D Materials and Applications (2022)6:39; <https://doi.org/10.1038/s41699-022-00316-6>

INTRODUCTION

Friction exists in almost all mechanical systems with moving parts and it accounts for about a third of the world's energy consumption^{1,2}. Consequently, friction is the process of energy dissipation when the surfaces of moving parts slide against each other. The friction reduction is desirable at all scales from macro to nano for saving energy^{3,4}. Atomically thin 2D materials such as graphene, transition metal dichalcogenides (e.g., MoS₂), and boron nitride (h-BN) exhibit excellent lubrication properties and attract wide attention as solid lubricants in confined layers of molecular thickness for various micro-and nanoelectromechanical systems (MEMS/NEMS)^{5–8}. Also, alternating hold and release the interfacial parts for steady operation in the control knob and sliding actuators of 2D materials-based MEMS/NEMS³ require controllable friction. It is necessary to not only seek the contributions but also the basic science such as energy dissipation to be understood to the friction on 2D materials effectively. The atomic force microscopy (AFM) methods have allowed basic studies of friction mechanisms on atomically thin 2D materials which intensively address how energy is dissipated at a sliding contact⁹.

There has been considerable progress in understanding the energy dissipation of friction on atomically thin 2D materials in the past few decades¹⁰. The structure^{11,12} and substrate^{13–15} affect the friction on atomically thin 2D materials deposited on the substrate due to the elastic deformation¹⁵, adhesion induced puckering¹⁶, and contact quality^{17,18}. The kinetic energy associated with the AFM tip sliding on atomically thin 2D materials could attribute to dissipation by coupling the atomic relaxations to phonon modes that propagate away and the elastic deformation energy due to the out of plane deformation^{16–18}. Then the defect generation and chemical functionalization of atomically thin 2D materials could tune the friction by increasing locally the potential corrugation and lowering the bending rigidity, but destroy the structure permanently^{19–21}. The friction on the surface of atomically thin graphene is reduced dramatically by enhancing interfacial

adhesion between graphene and supporting SiO₂/Si substrate via plasma treatment of the substrate to suppress the puckering effect^{16,22}. However, the tuning of the friction on atomically thin graphene is irreversible because the interfacial bonding is hard to recover to the initial state²³. The friction on monolayer graphene can be modulated reversibly by tuning the atomic-level contact quality with simple mechanical straining under the relatively small range of applied load¹⁸. In a word, the energy dissipation of friction on atomically thin 2D materials is still undefined for controllable tuning.

The sliding AFM tip during friction involves the direct transfer of energy into the phononic dissipation and electron-hole pairs before transfer to the phonon populations. The electron-phonon coupling (EPC) becomes another channel for energy dissipation and builds a link between electronic and phononic effects¹². Consequently, the energy of friction can be dissipated through phononic consumption and electronic contribution^{24–26}. Electronic contributions to energy dissipation of friction on atomically thin 2D materials need to be manifested in many physical phenomena. Dong²⁷ quantitatively calculated the effect of EPC on the friction of monolayer graphene by MD simulation with a Langevin equation and found the friction increases slightly with the increase of EPC. Filleter et al.¹² found that the nanofriction on monolayer graphene was twice than that on bilayer graphene due to the strong EPC in monolayer graphene by means of angle-resolved photoemission spectroscopy. While a deep understanding of the EPC affects the frictional properties of 2D materials in essence is still required. Park et al.²⁸ discovered that the accumulation of carriers near the semiconducting surface leads to excess friction due to high carrier density. Furthermore, the electron doping for single-layer and bilayer graphene transistors has been investigated with non-destructive Raman spectroscopy characterization based on the renormalization of the G and 2D modes as a function of carrier concentration²⁹. However, the electronic contribution to friction during sliding contacts provides

¹College of Mechanical Engineering, Donghua University, Shanghai 201620, China. ²Shanghai Collaborative Innovation Center for High Performance Fiber Composites, Donghua University, Shanghai 201620, China. ✉email: yitianpeng@dhu.edu.cn

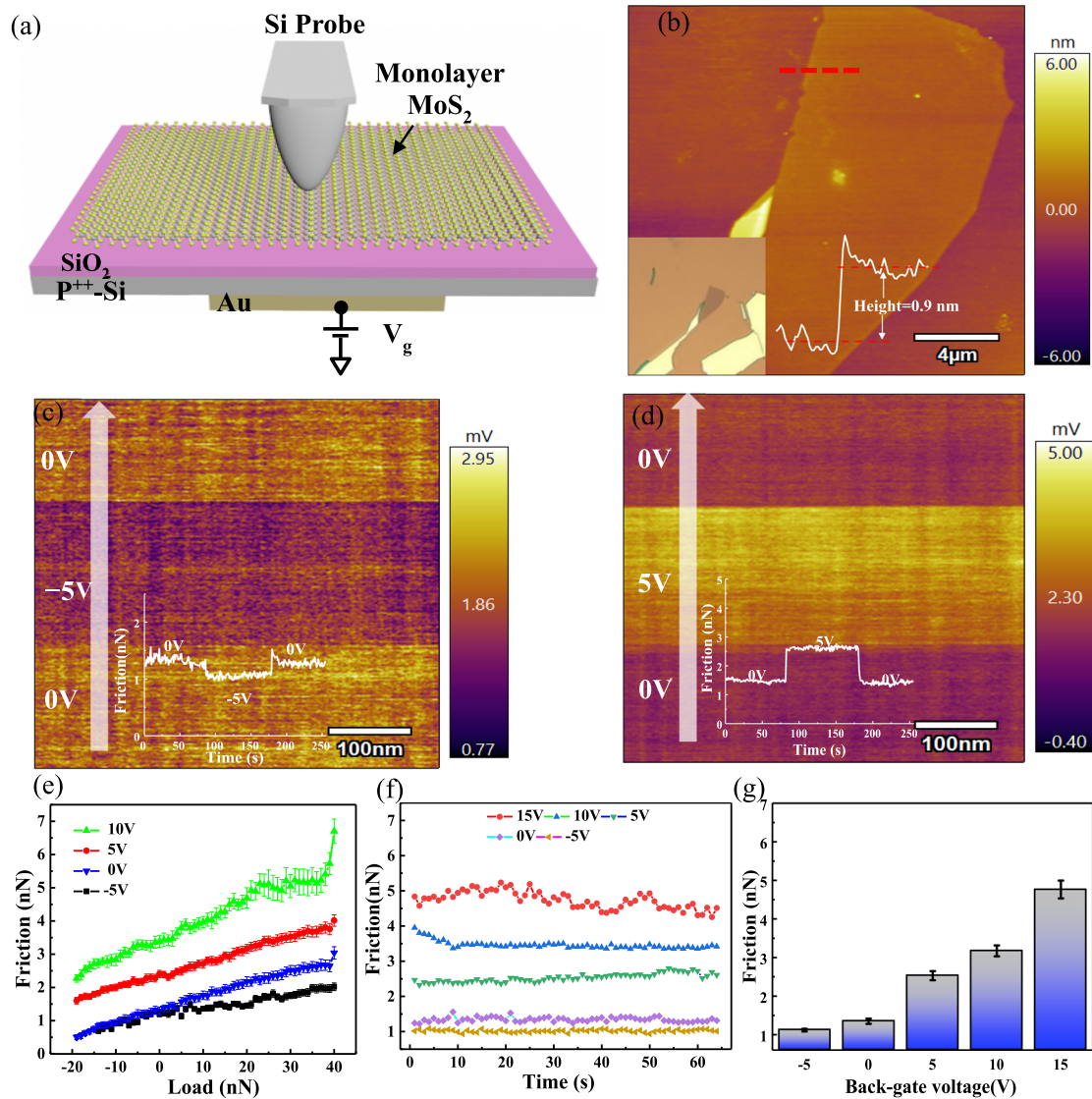


Fig. 1 The nanofriction experiments under different V_g . **a** Schematic of the nanofriction measurements on atomically thin MoS₂ under different V_g . **b** AFM image and optical image (inset) of atomically thin MoS₂ including the height profile of atomically thin MoS₂ along the red dash line (inset). Scale bar: 2 μm . **c** Friction map with the applied load of 10 nN under the modulation of V_g from 0 V to -5 V and back to 0 V. The inset shows the profiles of the nanofriction indicated by the white arrow line. Scale bar: 100 nm. **d** Friction map with the applied load of 10 nN under the modulation of V_g from 0 V to 5 V, then back to 0 V. The inset shows the profiles of the nanofriction indicated by the white arrow line. Scale bar: 100 nm. **e** The nanofriction on atomically thin MoS₂ as a function of applied load with different V_g . **f** The nanofriction at a constant load of 10 nN under different V_g . **g** The nanofriction on atomically thin MoS₂ varied with the different V_g . Error bars represent standard deviations.

a possible method to tune the friction on atomically thin 2D materials through the carrier concentration³⁰.

The semiconductor materials offer an interesting platform to investigate the electronic contribution to energy dissipation where energy dissipation is linked to interaction with the electron system. The charge carrier concentration and energy band alignment of semiconductors could be extensively and precisely controlled by the electric field³¹. In contrast to the zero gaps of graphene and wide gap of boron nitride³², mechanically exfoliated atomically thin MoS₂ exhibits unique n-type semiconducting properties and tunable bandgap³³. The carrier concentration in atomically thin MoS₂ can be modulated easily with high sensitivity in a relatively large range from $\sim 10^{13}$ to 10^{15} cm^{-2} by many orders of magnitude using the gate voltage^{34,35}. Atomically thin MoS₂ with semiconductive properties provides the possibility to study the effect of free charge carriers in the energy dissipation of friction because it is possible to reversibly change their density

over many orders of magnitude. Scanning Kelvin force microscopy (SKPM) has been used to measure the contact potential difference (CPD) of atomically thin MoS₂ under the gate voltage to calculate the variation of carrier concentration during the carrier accumulation and depletion^{36,37}. The strengthening degree of EPC on atomically thin MoS₂ could be detected by the Raman spectra. As the degree of EPC correlated strongly with carrier concentration, the potential distribution of atomically thin MoS₂ provides the connection of carrier concentration with energy dissipation based on the modulation of gate voltage³⁸. Then, the friction on atomically thin MoS₂ could be tuned by regulation of the carrier concentration over many orders of magnitude based on field effect.

In this manuscript, the carrier concentration of atomically thin MoS₂ deposited on SiO₂/Si substrate is controlled by gate voltage (V_g) based on field effect. Then the electronic friction and energy dissipation on atomically thin MoS₂ are investigated by

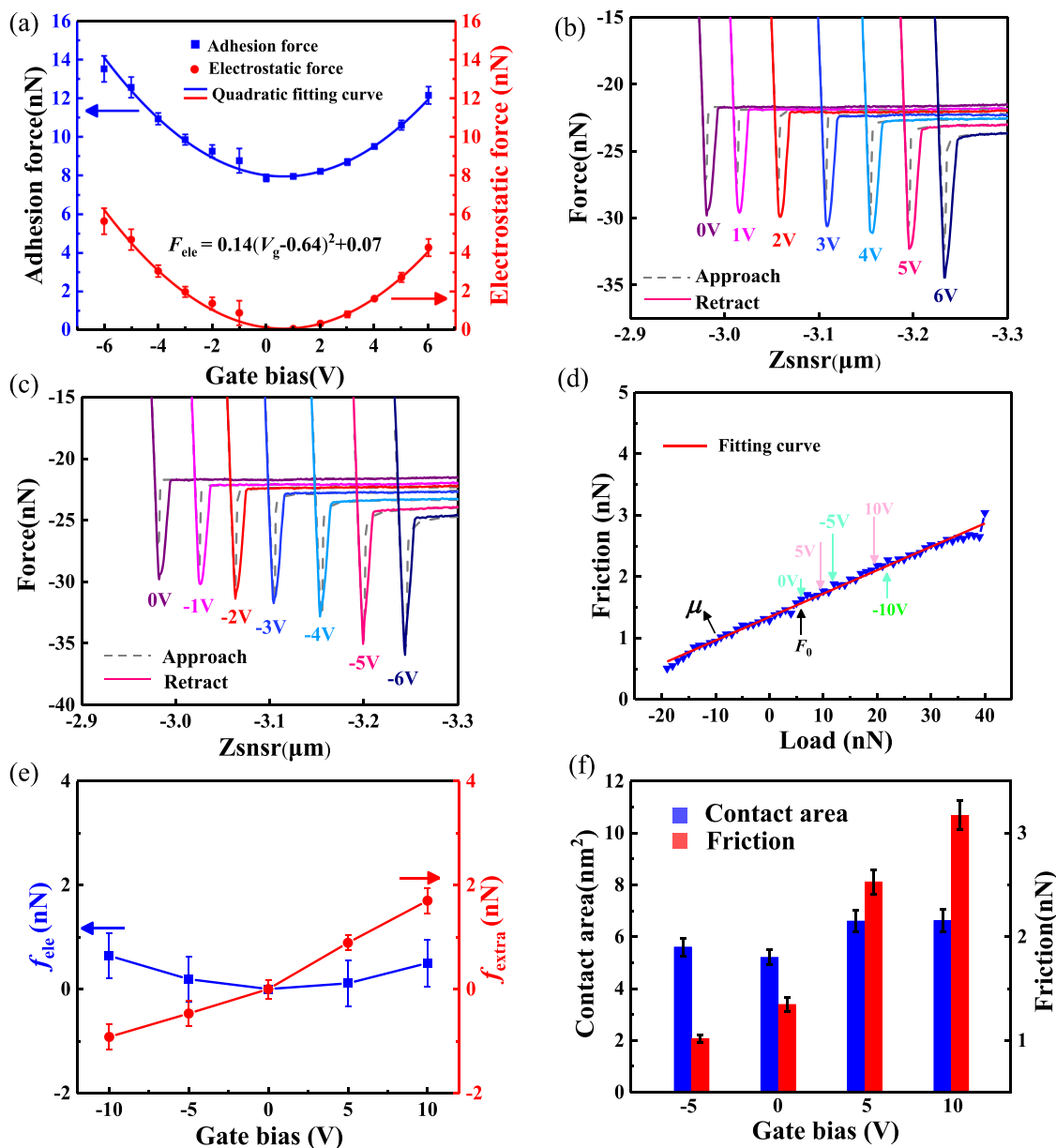


Fig. 2 Force-distance curves on atomically thin MoS₂ and variation of contact area under different V_g. **a** Adhesion and electrostatic force as a function of V_g. **b** Typical force-distance curves measured under the positive V_g. **c** Typical force-distance curves measured under the negative V_g. **d** Plots of the friction force versus the applied load on atomically thin MoS₂ at V_g = 0 V. **e** The nanofriction caused by electrostatic force (f_{elec}) and additional effect (f_{extra}). **f** Variation of the true contact area during AFM tip sliding on atomically thin MoS₂ under different V_g. Error bars represent standard deviations.

modulating the degree of EPC with varying carrier concentration based on atomic-scale stick-slip calculation, surface potential, and in-situ Raman spectroscopy under the external electric field. The friction on atomically thin MoS₂ is tuned dynamically, repeatedly, and controllably based on the modulation of the carrier concentration further.

RESULTS AND DISCUSSION

Friction properties under the electric field

The topography of the atomically thin MoS₂ on SiO₂/Si substrate acquired by AFM in tapping mode is shown in Fig. 1b. The height of atomically thin MoS₂ is about 0.9 nm corresponding to a single layer from the topography profile in the inset of Fig. 1b. Then, the nanofriction of atomically thin MoS₂ deposited on SiO₂/Si

substrate was investigated using calibrated AFM under the gate voltage, as schematically shown in Fig. 1a. As shown in Fig. 1c, the V_g was sequentially applied in the order of 0—5 V and then return to 0 V. The nanofriction on atomically thin MoS₂ decreases at V_g = -5 V and then recovered fully to its initial state when V_g was returned to 0 V. The nanofriction has little change under relatively low negative V_g < -5 V (Supplementary Information Fig. 1). The nanofriction on atomically thin MoS₂ at V_g = -5 V decreases about 20% contrast to the initial value from Fig. 1c. The nanofriction on atomically thin MoS₂ is reduced obviously at the negative gate voltage of -5 V and decreases slightly with the increase of the negative bias when the gate voltage is beyond -5 V. However, the nanofriction on atomically thin MoS₂ under the V_g = 5 V increases almost to 1.8 times than the initial value, as shown in Fig. 1d. The nanofriction on atomically thin MoS₂ increases with the increase

of positive gate voltage from 0 to 5 V, then recovered fully to its initial value when V_g was returned to 0 V, as shown in Fig. 1d. Therefore, the nanofriction on atomically thin MoS₂ can be reversibly tuned by the regulation of V_g . Also, the polarity of the applied V_g exhibits a different effect on the nanofriction of atomically thin MoS₂. Figure 1e shows the curves of nanofriction on atomically thin MoS₂ versus the applied load measured under different V_g . Figure 1f shows the nanofriction on atomically thin MoS₂ at a constant load of 10 nN under different V_g . The corresponding relationship between the magnitude of nanofriction and the applied V_g is shown in Fig. 1g. The high-resolution AFM image of atomically thin MoS₂ denotes that it can remain stable after the friction test under the external electric field (Supplementary Information Fig. 2). It can be clearly seen that the nanofriction on atomically thin MoS₂ was affected by the direction and magnitude of the V_g .

Mechanism

The adhesion on atomically thin MoS₂ were measured using AFM under different V_g . Figure 2a shows the adhesive force on atomically thin MoS₂ and electrostatic force as a function of the V_g . The adhesion F_{ad} approximately follows a parabolic law, i.e., $F_{ad} \propto V^2$, with little difference between positive and negative V_g . The F_{ad} mainly consists of van der Waals force (F_{vdW}), electrostatic force (F_{ele}), capillary force (F_{cap}), and chemical bonding force (F_{chem}) in an ambient environment, which can be written as:

$$F_{ad} = F_{vdW} + F_{ele} + F_{cap} + F_{chem} \quad (1)$$

The surface properties of mechanically exfoliated atomically thin MoS₂ keep highly hydrophobic and stable with barely dangling bonds under different V_g (Supplementary Information Fig. 3). Also, any effect of a changing tip structure, geometrically or chemically can be neglected during the nanofriction experiment under different V_g . The change of F_{vdW} , F_{cap} , and F_{chem} can be neglected for the increase of the adhesion between the AFM tip and atomically thin MoS₂ under different V_g . Consequently, the main reason for the change of adhesion force is the effect of F_{ele} under different V_g . The electrostatic force caused by the electric field could be quantitatively calculated from the adhesion measurement of the single force curve under different V_g . So the F_{ele} can be calculated using Eq. (1) at different V_g , as shown in Fig. 2a. Based on the quadratic fit of the electrostatic force, the relationship between the F_{ele} and the V_g is

$$F_{ele} = 0.14(V_g - 0.64)^2 + 0.07 \quad (2)$$

The electrostatic forces at $V_g = 0$ V, 5 V, 10 V, -5 V and -10 V are about 0 nN, 2.73 nN, 12.4 nN, 4.69 nN and 15.92 nN, respectively. The electrostatic force would increase the interaction between the tip and the atomically thin MoS₂ and create additional friction. Therefore, the additional nanofriction (f_{ele}) caused by F_{ele} was calculated while the F_{ele} was treated as an additional load to the AFM tip. The typical single force curves on the atomically thin MoS₂ were acquired with the AFM tip under the positive V_g , as shown in Fig. 2b. The difference of pull-off force between 0 V and 6 V reveals the attraction contact because of the electrostatic interaction. The typical single force curves on the atomically thin MoS₂ under the negative V_g shown in Fig. 2c have a similar tendency as the positive V_g .

The initial value of nanofriction starts with the adhesion force of 7.8 nN and the corresponding normal load is also 7.8 nN. Therefore, f_{ele} can be given by

$$f_{ele} = \mu \times F_{ele} \quad (3)$$

where μ is defined as the equal friction coefficient fitted from the friction as a function of load, as shown in Fig. 2d. The values of f_{ele} were calculated approximately to be 0 nN, 0.11 nN, 0.50 nN,

0.19 nN, and 0.64 nN at the V_g of 0 V, 5 V, 10 V, -5 V, and -10 V, respectively. Consequently, the increases of the nanofriction under different V_g are far more than the additional f_{ele} caused by electrostatic force. It can be concluded that there is an additional effect leading to the nanofriction increasing. Therefore, the nanofriction (f_{extra}) caused by the additional action can be given by the equation:

$$f_{extra} = f_g - f_{ele} - f_0 \quad (4)$$

where f_0 is the nanofriction at $V_g = 0$ V, f_g is the nanofriction force under the different V_g with the applied load of 7.8 nN. The force of electrostatic attraction was supposed to increase the adhesion force, then increase nanofriction under the normal electric field. Figure 2e also shows that the electrostatic force is insufficient to increase the nanofriction to such an extent. Consequently, there is an additional mechanism for the increase on the nanofriction but the load. Considering that the change of adhesion force is closely related to the change of contact area, the nanofriction usually agrees well with the true contact area based on the contact model of Derjaguin-Müller-Toporov (DMT). As shown in Fig. 2f, the changes of contact area between the AFM tip and atomically thin MoS₂ (Detailed calculation process in Supplementary Information Fig. 4) could not account for the obvious variation in nanofriction under different V_g . These findings indicate that the f_{ele} plays a small role in the change of nanofriction on atomically thin MoS₂ under the different V_g . Meanwhile, the gate voltage induced another factor to change the nanofriction on atomically thin MoS₂ besides the contact area.

The atomic-scale stick-slip behaviors on atomically thin MoS₂ were measured using AFM to comprehend the underlying mechanism under different V_g further. The lateral force curves at atomic scale under different V_g are shown in Fig. 3a. The sawtooth shape of the trace shows the atomic lattice period of about 0.31 nm corresponding to the lattice constant of atomically thin MoS₂. It is also clearly observed that the distance of the stick-slip period increases from 0.31 nm to 0.87 nm when the V_g was regulated from 0 V to 4 V. The atomic-level stick-slip behaviors of the lateral force on atomically thin MoS₂ change with V_g , then return to the original. As the V_g increased, the stick-slip behaviors switch from single-slip to multiple-slip regime. The multiple-slip regime can also be fully recovered to a single-slip regime when V_g returns from 4 V to 0 V, as shown in Fig. 3a. The reversible transition between single slip and multiple slips indicates that the atomic-scale stick-slip behaviors can be reversibly modulated by the V_g . The lateral force map in the sliding process under different V_g is shown in Fig. 3b. Figure 3b was used to analyze the lateral force map in the sliding process under different gate voltages. Figure 3b indicated that the multiple-slip regime can also be fully recovered to a single-slip regime when V_g changes from 0 V to 6 V and then return to 0 V. Few regular atomic stick-slip motions are also observed when $V_g \geq 6$ V (Supplementary Information Fig. 5). As shown in Fig. 3c, the mean lateral force increases with the increase of V_g . In the meantime, the total energy dissipation calculated from the atomic-scale stick-slip curves increased monotonically with the increase of the positive V_g shown in Fig. 3c. In addition, the distance between the trace and retrace values decreases demonstrating less energy dissipation for the decrease of average nanofriction under the negative V_g .

The increase in the lateral force of stick-slip asymmetry suggests an incremental energy corrugation (see Supplementary Information Fig. 6)³⁹. Therefore, a large lateral force is required to cross the barrier resulting in more energy dissipation under the positive V_g . The lateral contact stiffness was extracted from the slope of each stick phase in lateral force curves at the atomic scale in Fig. 3a. It has been reported that the value of lateral contact stiffness increases with load, indicating the increase of the contact area⁴⁰. However, Fig. 3d shows that the lateral contact stiffness is almost kept stable under different V_g at a given load. Generally, the lateral

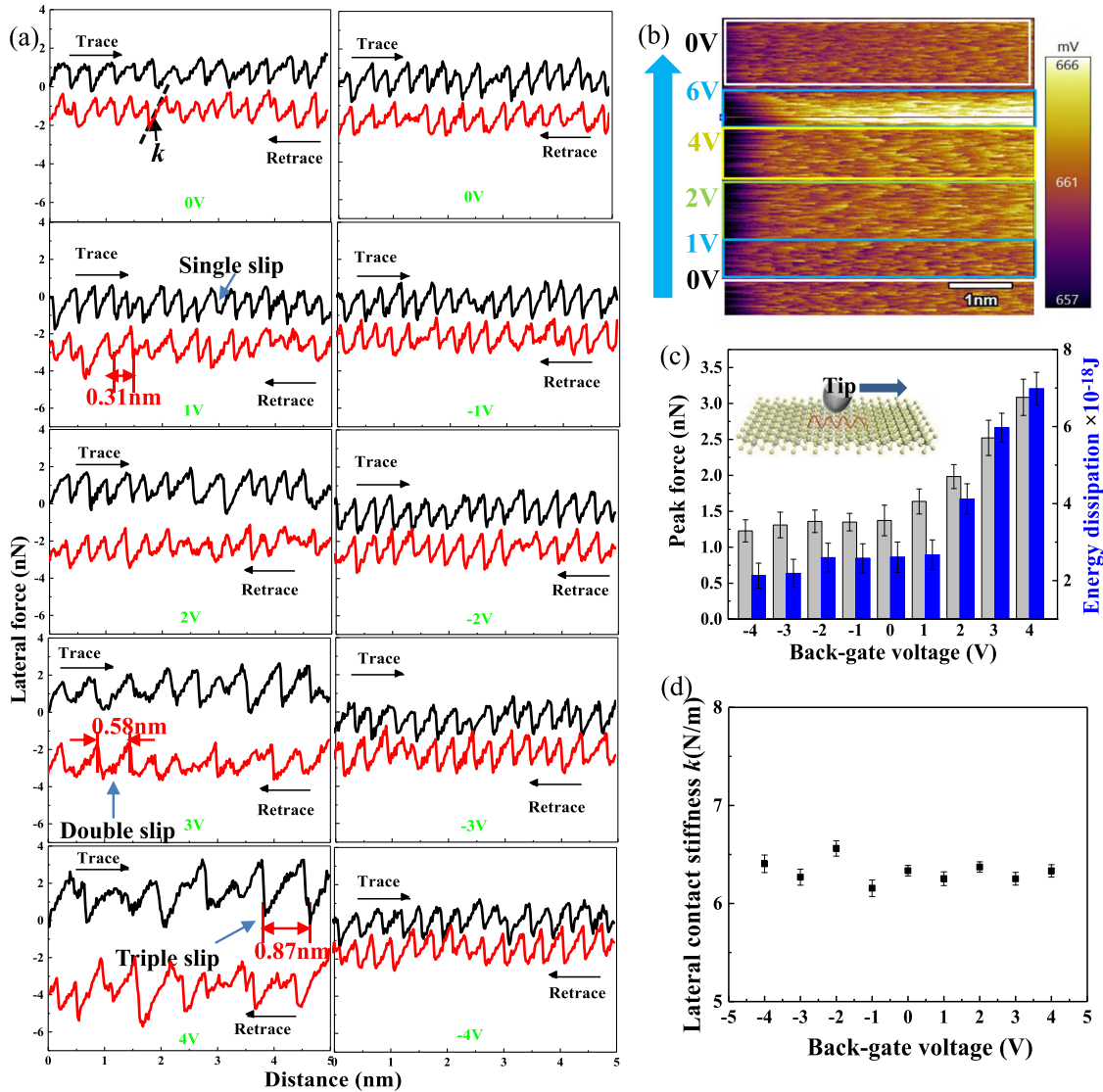


Fig. 3 Atomic-scale friction and stick-slip behavior on atomically thin MoS₂ under different V_g. **a** Stick-slip behavior measured at V_g = -4 to +4 V, respectively. **b** Lateral force mapping under different V_g; the gate bias voltage was dynamically modulated from 0 V to 6 V and return to 0 V. Scale bar: 1 nm. **c** Energy dissipation and lateral peak force under different V_g. **d** The lateral contact stiffness *k* under different V_g. Error bars represent standard deviations.

contact stiffness would show a prominent deviation by the sliding energy barrier⁴¹. In addition, the average shear stress of the contact was analyzed. The friction (*F*) is proportional to the real contact area (*A*) as $F = \tau \times A$ ⁴¹, where τ is the shear strength. The real contact area under different gate voltages has been obtained based on the DMT model shown in Fig. 2f. The variation of the contact area and shear strength with gate voltages is shown in Supplementary Fig. 7 (see Supplementary Information). The shear strength increases under the positive gate voltages and decreases under the negative gate voltages. However, the data in Fig. 3 shows that the contact stiffness remains unchanged under different bias voltages. The reason is that Formula (1) holds if electronic contributions to friction are not involved²⁸. These results indicated that the shear stress is hard to explain the experimental results of MoS₂ under the electric field. Consequently, the variation of nanofriction on atomically thin MoS₂ at different V_g can attribute to another factor beyond the energy dissipation from the energy barrier.

In addition to the changes in electrostatic force between the tip and atomically thin MoS₂ under the external electric field, a more

trivial effect of the V_g is to modulate the carrier concentration based on the electric field effect⁴². The carrier concentration can be calculated based on $n = N_c \exp\left(\frac{-(E_c - E_f)}{k_B T}\right)$ ^{43,44}, where $N_c = (2m^*)/(\pi\hbar^2) = 3.8 \times 10^{14} \text{ eV cm}^{-2}$ is the density of states in the conduction band, E_c is the bottom of the conduction band, k_B is Boltzmann constant ($k_B = 1.380649 \times 10^{-23} \text{ J/K}$), T is the temperature (300 K), E_f is the Fermi energy level. E_f can be calculated by measuring the surface potential through SKPM. Therefore, the SKPM test is used to calculate the carrier concentration of MoS₂. The work function of MoS₂ can be calculated by SKPM based on the formula of $\Delta\text{CPD} = (W_{\text{tip}} - W_{\text{sample}})/e$ ⁴⁵, where W_{sample} and W_{tip} are the work functions of the MoS₂ and tip, e is the electronic charge. The work function of MoS₂ can be calculated by measuring ΔCPD with SKPM, and then the Fermi energy level of MoS₂ can be calculated by $W = 0 - E_f$. However, the surface potential of MoS₂ is not only determined by the work function of MoS₂ but also directly affected by the electric field after applying the gate voltage. The surface potential of SiO₂ under the different V_g was measured and the results are shown in

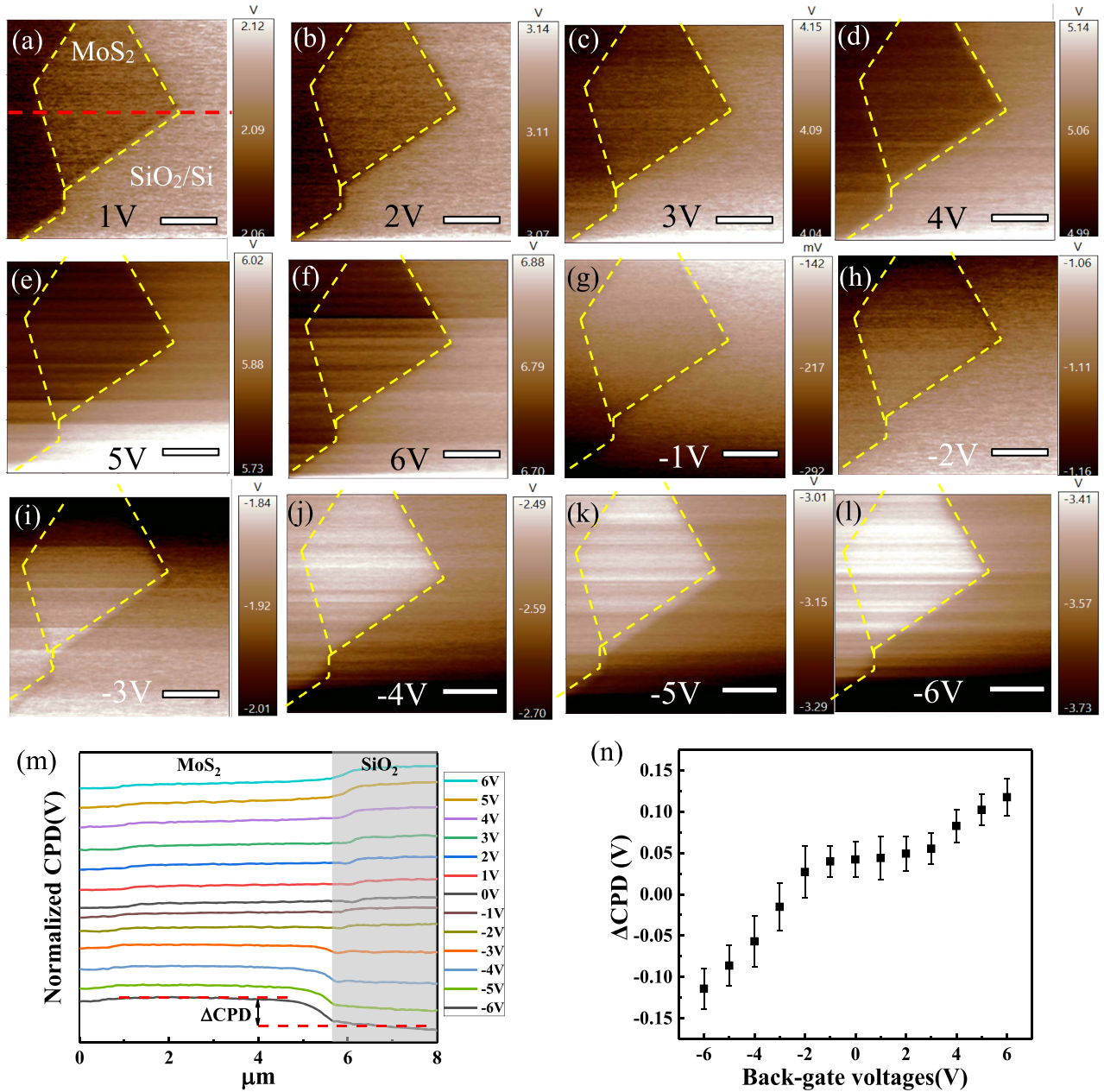


Fig. 4 Surface potential mapping of atomically thin MoS₂ on SiO₂/Si substrate. **a–l** The surface potential mapping of atomically thin MoS₂ under different V_g : -6 – $+6$ V. Scale bar: 2 μ m. **m** The line profiles of surface potential along the white line across the atomically thin MoS₂ under different V_g . **n** Δ CPD of atomically thin MoS₂ as a function of V_g . Error bars represent standard deviations.

Supplementary Fig. 8 (Supplementary Information). To minimize the influence of the applied electric field on the SKPM test, the surface potential of SiO₂ was used as the reference. Because the relationship between the surface potential of SiO₂ and gate voltage is linear. The surface potential of SiO₂ is consistent with the V_g indicating that the work function of SiO₂ as an insulator is very little affected by the V_g . Therefore, the surface potential difference between SiO₂ and MoS₂ (Δ CPD) was used to reflect the effect of electric field on MoS₂, which is relatively more accurate. The surface potential of MoS₂ deposited on SiO₂/Si substrate under different V_g was shown in Fig. 4a–l. The yellow dotted box denotes the area of the atomically thin MoS₂ on the surrounding SiO₂/Si substrate. The surface potential of atomically thin MoS₂ increases with the increase of positive V_g as presented in Fig. 4a–f. Also, the surface potential of atomically thin MoS₂ decreases with a decrease of the negative V_g , as shown in Fig. 4h–l. The potential

of MoS₂ is lower than the potential of SiO₂ under the positive gate voltages indicating that the MoS₂ is an n-type semiconductor, while the potential of MoS₂ is higher than the potential of SiO₂ under the negative gate voltages indicating that the n region is reverse-biased causing depletion or weak inversion³⁶. Surface potential profiles along the atomically thin MoS₂ on the SiO₂/Si substrate under the different V_g are shown in Fig. 4m. The values of Δ CPD are given in Fig. 4n after applied gate voltage from -6 to $+6$ V. Therefore, the carrier concentration was calculated based on $n = N_c \exp\left(\frac{-(E_c - E_f)}{k_B T}\right)$, where $E_c = -3.92$ ⁴⁶, $k_B T = 0.0259$ eV⁴⁷, $E_f = -W_{\text{sample}}$. The work function of conductive tip is 4.29 eV. The Δ CPD is 0.043 V at the gate voltage of 0V and the corresponding Fermi energy level is $E_f = -4.22$. The Δ CPD is 0.102 V at the gate voltage of 5V and the corresponding Fermi energy level is $E_f = -4.13$. Therefore, the carrier concentration of MoS₂ is 3.4×10^9

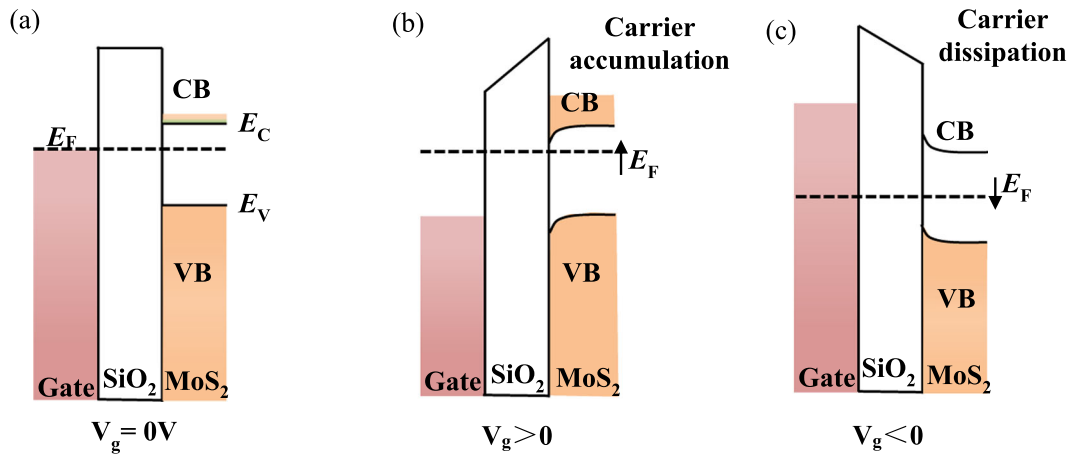


Fig. 5 Energy band diagram of atomically thin MoS₂ with n-type semiconductor properties. **a** Energy band diagrams of atomically thin MoS₂ at equilibrium. **b** The energy band bending and electron accumulation caused by the existence of donor-like surface states under the positive gate voltage. The band diagram of the MoS₂/SiO₂/Si structure. **c** The band diagram of the MoS₂/SiO₂/Si structure at negative gate voltage. The energy band bending and surface electron depletion under the negative gate voltage.

cm^{-2} at the gate voltage of 0 V (intrinsic carrier concentration) and $0.12 \times 10^{12} \text{cm}^{-2}$ at the gate voltage of 5 V. Carrier concentration n can also be approximately calculated using the idealized parallel-plate capacitor model with $n = C_{\text{SiO}_2} \times V_g$ (C_{SiO_2} is $\sim 15 \text{ nF cm}^{-2}$ for 300 nm SiO₂ dielectrics)⁴⁸. Therefore, the alternate surface potential of atomically thin MoS₂ suggests that the carriers accumulate under the positive V_g and dissipate under the negative V_g from the surface potential characterization and calculation.

The variation of the CPD also indicates the direction and amount of energy band bending and the position of the Fermi level at the surface caused by surface electron states⁴⁹. Since the atomically thin MoS₂ is n-type semiconductor, the Fermi level in equilibrium is close to the conduction band (CB), as shown in Fig. 5a. The energy band bends downward and Fermi level is closer to the conduction band under the positive V_g . When a positive V_g is applied, only a few tenths of electron-volts shift at the conduction band edge⁵⁰. This effect is clearly observed in Fig. 4n, where a positive V_g results in a little increase of ΔCPD due to its proximity to CB. However, the change of Fermi level under the negative is significantly changed due to the large distance between the Fermi level and the valence band (VB), as shown in Fig. 5c. Therefore, a large increase in ΔCPD was observed under the negative V_g . Furthermore, the variation in carrier concentration contributes to the shift of the position of Fermi level by the band bending. The energy band of atomically thin MoS₂ bends downward and the Fermi level is closer to the conduction band resulting in carrier accumulation under a positive V_g . Figure 5c shows that the energy band bends upward and the Fermi level is closer to the valence band under the negative V_g , indicating that the carrier dissipates near the atomically thin MoS₂ surface.

Although the surface potential decreases significantly under the negative V_g , the corresponding carrier concentration decreases slightly. Similarly, the friction (or peak force) in Fig. 3c also shows a slight decrease as the voltage increases from 0 V to -4 V. Therefore, the decrease of ΔCPD in Fig. 4n indicates that the carrier concentration decreases under the negative gate voltage. Therefore, the decrease of carrier concentration under the negative V_g may be closely related to the decrease of nanofriction.

The nondestructive characterization of in-situ Raman spectroscopy was explored to investigate the effect of carrier concentration on the EPC on atomically thin MoS₂ under different V_g . The schematic diagram of Raman spectroscopy analysis on the gate-modulated carrier concentration of

atomically thin MoS₂ was depicted in Fig. 6a. Figure 6b displays the evolution of zone-center phonon E_{12g}^1 and A_{1g} modes of the atomically thin MoS₂ under different V_g . As depicted in the inset of Fig. 6b, the A_{1g} phonon involves the sulfur atomic vibration in the opposite direction along the c axis (perpendicular to the basal plane), whereas the E_{12g}^1 mode illustrates the displacement of Mo and S atoms in the basal plane. The dependence of the change in different renormalization mode frequencies of the two modes A_{1g} and E_{12g}^1 on the carrier concentration from the obtained Line-shape parameters show that the A_{1g} mode frequency softens by 4 cm^{-1} , as compared to only $\sim 0.6 \text{ cm}^{-1}$ for the E_{12g}^1 mode under the maximum voltage of 20 V. The linewidth of the A_{1g} mode increases significantly by $\sim 0.98 \text{ cm}^{-1}$ for the maximum doping achieved, whereas the linewidth of the E_{12g}^1 mode does not show appreciable change. The renormalization A_{1g} mode could be used as a sign of the quantitative EPC corresponding to the carrier concentration modulated by the V_g . The down-shift of A_{1g} mode is due to the increase of carrier concentration leading to the occupation of an anti-bonding state in the conduction band of atomically thin MoS₂. The occupation of an anti-bonding state increases the total electron energy of the system and weakens the Mo-S bond due to electron doping. Therefore, electron doping caused a significant change in the EPC of the A_{1g} mode, while the E_{12g}^1 mode of Raman spectra with symmetry is quite insensitive to the external electric field. The phonon frequency and linewidth of the E_{12g}^1 mode are much less dependent on carrier concentration. Figure 6c, d show the shift of the mode frequencies and the corresponding full width at half maximum (FWHM) as a function of V_g , respectively. The A_{1g} mode specifically exhibits a strong sensitivity to electron doping and the phonon frequency decreases by 4 cm^{-1} and the linewidth broadens by 1.1 cm^{-1} for electron doping at the V_g of 20 V. The FWHM of Raman mode derives from three factors as given below: $\Gamma_{\text{FWHM}} = \Gamma_0 + \Gamma_{\text{anh}} + \Gamma_{\text{EPC}}$, where Γ_0 is the intrinsic FWHM, Γ_{anh} denotes the phonon-phonon interaction, and Γ_{EPC} is due to EPC⁵¹. Therefore, the Γ_{EPC} can be used to illustrate the strength degree of EPC. The Γ_0 and Γ_{anh} are expected to be the same at different V_g . The FWHM of A_{1g} mode increases with the increase of carrier concentration. However, the FWHM of the E_{12g}^1 phonon was independent of the electron concentration³⁸. The high level of carrier concentration causes the strong strength of EPC from the change in the A_{1g} . The Γ_{EPC} increases with the increased carrier concentration indicating that the strength of EPC increases with the increased carrier concentration. The friction increases with the increase of the carrier concentration,

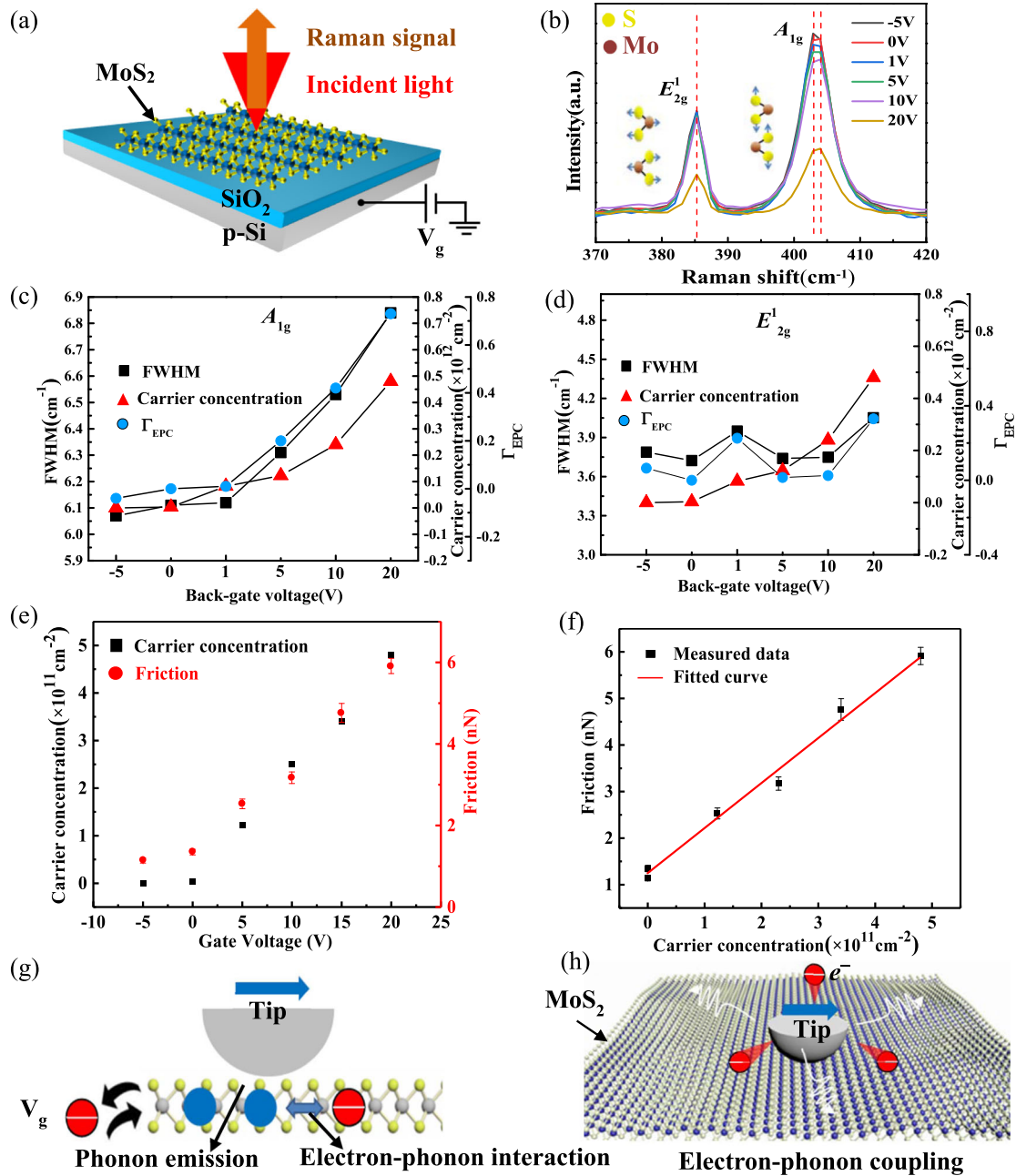


Fig. 6 The influence of normal electric field on nanofriction using Raman spectroscopy. **a** Raman experimental setup. **b** Raman spectra of atomically thin MoS₂ under different V_g . **c** FWHM and carrier concentration of A_{1g} mode as a function of V_g . **d** FWHM and carrier concentration of E_{2g}^1 mode as a function of V_g . **e** Carrier concentration and friction as a function of gate voltage. **f** Plots of the friction as a function of carrier concentration. **g** AFM tip sliding on atomically thin MoS₂ emitting electron and phonon pairs. **h** Schematic diagram of the energy dissipation as the AFM tip slides on atomically thin MoS₂. Error bars represent standard deviations.

indicating that the energy dissipation of friction is consistent with the strengthening of EPC. Both the friction and carrier concentration increase with the increase of gate voltage confirming a strong correlation between the friction and carrier concentration from Fig. 6e. The data of friction and carrier concentration were fitted to quantify the relationship between the friction and carrier concentration. The fitted curve in Fig. 6f shows that the relationship between the friction (F) and carrier concentration (n_e) is

$$F = 0.97n_e + 1.23 \quad (5)$$

Therefore, the friction to the carrier concentration approximately follows a linear function of one variable.

Figure 6g shows the schematic diagram of the energy dissipation as the AFM tip slides on atomically thin MoS₂ emitting phonon. The phonons produced by friction on atomically thin MoS₂ interact with electrons and lead to an additional channel of energy dissipation by EPC, as schematically shown in Fig. 6h. Therefore, the strength of EPC in atomically thin MoS₂ was significantly changed by the gate-modulated carrier concentration. The physical picture for the change in nanofriction on atomically thin MoS₂ under different

V_g was proposed: the instability of the stick-slip behavior would cause local vibration of the crystal lattice and the vibration energy is dissipated by the excitation and propagation of phonons. However, the associated lattice motion is damped by the creation of electronic excitations through EPC in atomically thin MoS₂ with high electron doping. Also, the EPC could change the dynamic behavior of lattice motion. The trajectory of a nucleus in atomically thin MoS₂ during the friction process follows a Langevin equation^{25,26}. Therefore, the generalization of the Langevin equation can be used to demonstrate the energy dissipation due to EPC with a friction term R_i and a random force ζ_i ^{25,52},

$$m_i \frac{\partial v_i}{\partial t} = F_i(t) - \sum R_i(t) v_i + \zeta_i(t) \quad (6)$$

where m_i is the atom mass, v_i is the velocity, $F_i(t)$ denotes the total force exerted on atom (mean force), and R_i is the friction term representing the strength of EPC. $\zeta_i(t)$ is a random fluctuating force and subject to the fluctuation-dissipation theorem⁵³. The random force $\zeta_i(t)$ can be solved with the equation of $\langle \zeta_i(t) \zeta_i(t') \rangle \geq 2m_i R_i k_B T_e \delta(t - t')$, where δ is the Dirac delta function. R_i can be given as follows:

$$R_i = \frac{m_i g_{ep}}{3Nk_B}, \quad (7)$$

N is the number of atoms. ζ_i is related to g_{ep} and g_{ep} is the EPC parameter⁵⁴, which is $g_{ep} = \frac{\pi^2 m_e C_s^2 n_e}{6\tau(T_e)T_e}$, where m_e is the effective electron mass, C_s is the speed of sound, n_e is the electrons density, and $\tau(T_e)$ is the electron relaxation time defined as the electron-phonon scattering time. The EPC parameter is proportional to the electron density. Based on the equation of (7), the friction can be given as,

$$R_i = \frac{m_i m_e \pi^2 C_s^2}{18k_B^2 N \tau(T_e) T_e} n_e \quad (8)$$

The total friction F_{total} could be divided into two parts including the electronic contribution and phononic consumption. The friction caused by phononic consumption F_{ph} could be described

as Equation: $F_{ph} = \frac{\pi A}{b^2 \omega} \left[E_0 + kT \ln \left(\frac{v}{v_0} \right) \right]$ ⁵⁵. Thus,

$$F_{total} = F_{EPC} + F_{ph} = \frac{m_i m_e \pi^2 C_s^2}{18k_B^2 N \tau(T_e) T_e} n_e \times v_i + \frac{\pi A}{b^2 \omega} \left[E_0 + kT \ln \left(\frac{v}{v_0} \right) \right] \quad (9)$$

The $\frac{m_i m_e \pi^2 C_s^2}{18k_B^2 N \tau(T_e) T_e} \times v_i$ remains the same as can be treated as a constant α because only the carrier concentration was modulated by the electric field and other parameters such as temperature and velocity were kept the same. Furthermore, the friction caused by phononic consumption also remains the same. Thus, the F_{ph} is also set as a constant $\beta = \frac{\pi A}{b^2 \omega} \left[E_0 + kT \ln \left(\frac{v}{v_0} \right) \right]$. Then the general formula of friction on atomically thin MoS₂ under the electric field could be described as follows,

$$F_{total} = \frac{m_i m_e \pi^2 C_s^2}{18k_B^2 N \tau(T_e) T_e} v_i \times n_e + \frac{\pi A}{b^2 \omega} \left[E_0 + kT \ln \left(\frac{v}{v_0} \right) \right] = \alpha n_e + \beta \quad (10)$$

If α and β are equal to 0.97 and 1.23, respectively. Then, the friction is linear with the carrier concentration from the Langevin equation which is in accordance with the fitting of friction and carrier concentration.

The strength of electron-phonon coupling in atomically thin MoS₂ increases with the increase of gate voltage due to electron doping. Therefore, this leads us to the most likely scenario to explain the increased nanofriction of atomically thin MoS₂ under the applied gate voltage. Phonons excited by the mechanical energy of the sliding tip in atomically thin MoS₂ are much more likely to scatter with electrons, introducing a more efficient means of dissipating energy¹². During the observed stick-slip motion, the lattice is locally distorted and released by the slipping probe tip transferring kinetic energy into lattice vibrations²⁶. For the atomically thin MoS₂ under the electric field, the lattice motion is damped by the creation of electronic excitations through electron-phonon coupling. This additional mechanism increases the efficiency of energy dissipation during slip events which are responsible for frictional energy losses.

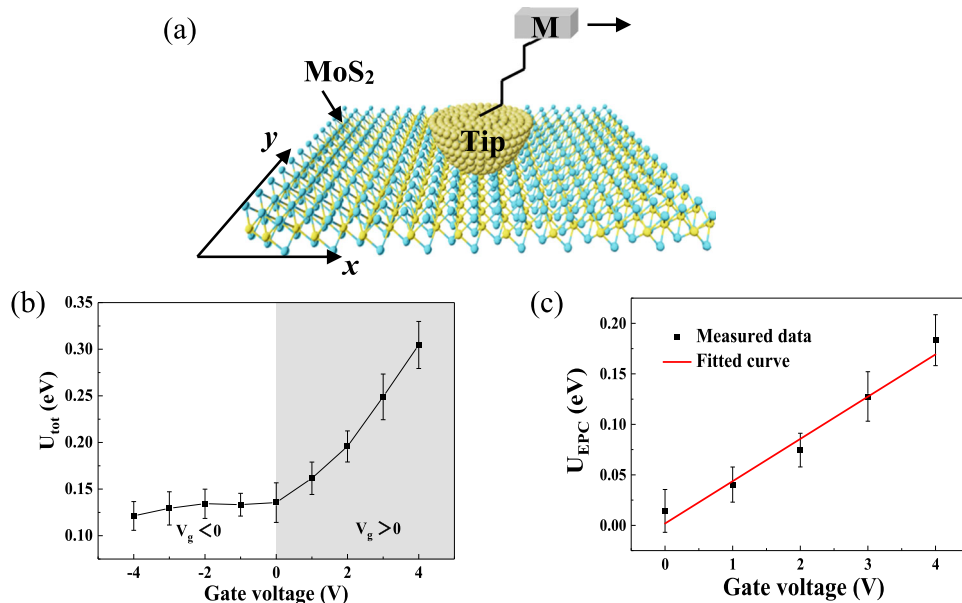


Fig. 7 Modified Prandtl–Tomlinson model and calculating of the energy corrugation. **a** Schematic of the modified Prandtl–Tomlinson model describing that the AFM tip moves on the monolayer MoS₂. **b** Energy corrugation U_{tot} as a function of gate voltage. **c** Energy corrugation U_{EPC} of electronic friction as a function of gate voltage. Error bars represent standard deviations.

The atomic-scale stick-slip curves under different gate voltages are shown in Fig. 3a. The Prandtl–Tomlinson model has been greatly accepted for depicting the universal stick-slip phenomena. Since only the carrier concentration is changed, the phononic friction is a constant under different gate voltages. We assume that a linear superposition of the phononic energy dissipation and an independent electronic friction channel caused by electron-phonon coupling (EPC)^{24,55}. Then, the total energy corrugation can be given by $U_{tot} = U_{ph} + U_{EPC}$, where U_{ph} is the energy corrugation of phononic friction, U_{EPC} is the energy corrugation of electric friction induced by EPC.

Therefore, a modified Prandtl–Tomlinson model was proposed, as shown in Fig. 7a. An AFM tip moves on MoS₂ surface can be simplified to the motion of a point mass being dragged over a periodic potential by a supporting body M through a spring. The elastic spring of stiffness k represents the torsional stiffness of the AFM cantilever. The system is characterized by the following potential energy^{56,57}:

$$V = -\frac{U_{ph} + U_{EPC}}{2} \cos\left(2\pi \frac{x_{tip}}{a}\right) + \frac{1}{2}k(x_{tip} - x_s)^2 \quad (11)$$

According to the modified PT model, the maximum lateral force F_{max} during the stick-slip motion is determined by the interface energy corrugation U_{ph} and U_{EPC} . The maximum of the absolute value of the force F_{max} is found at $x_{tip} = a/4$, and we obtain

$$U_{tot} = a \times F_L^{max} / \pi \quad (12)$$

The U_{tot} was shown in Fig. 7b. The U_{tot} increases significantly under the positive gate voltage and decreases slightly under the negative gate voltage. When the gate voltage is below 0V, the electronic friction was suppressed due to the dissipation of charge carriers and the phonon dissipation is governed by the energy

dissipation of friction. Therefore, the energy corrugation at -4 V is approximated as the U_{ph} . For a better analysis of the electronic friction branch, we subtract the U_{ph} curve from the total U_{tot} . What remains is the electronic friction contribution as a function of gate voltage in Fig. 7c. By fitting the U_{EPC} as a linear function of the gate voltage, we find that the relationship between the energy corrugation of U_{EPC} and the gate voltage is linear, which is consistent with the relationship between carrier concentration and friction.

The friction tuning effect induced by an electric current was investigated using conductive atomic force microscopy and DFT calculation by Song et al.⁵⁸. DFT calculations propose that a larger electron density fluctuation during sliding tends to have a larger sliding barrier change resulting in a larger change of friction, which confirmed the contribution of electron density fluctuation to friction. The carrier concentration of MoS₂ was tuned based on field effect modulation. Increasing carrier concentrations would increase the electron density fluctuation resulting in larger friction. Wang et al. has performed friction experiments of a single-asperity sliding on a high-T_c superconductor from 40 to 300 kelvin and they found that the electronic friction exceeds 50% of the total friction signal²⁴. Friction on single-layer graphene is found to be a factor of two larger than on bilayer films due to the electron-phonon coupling¹². In our manuscript, the phonon dissipation is governed by the energy dissipation of friction as the gate voltage is below 0V due to electron dissipation. The friction could be reduced by 17% under the negative voltage. Also, the nanofriction does not decrease further when the gate voltage exceeds -5 V. As a result, we infer that the electronic friction at the gate voltage of 0V is $\sim 17\%$ and phononic friction 83%. In addition, the charge carriers accumulate and the electron-phonon coupling is enhanced under the positive gate voltage, leading to more efficient energy dissipation due to electron doping. As a result, the electronic contribution dominates the energy dissipation in

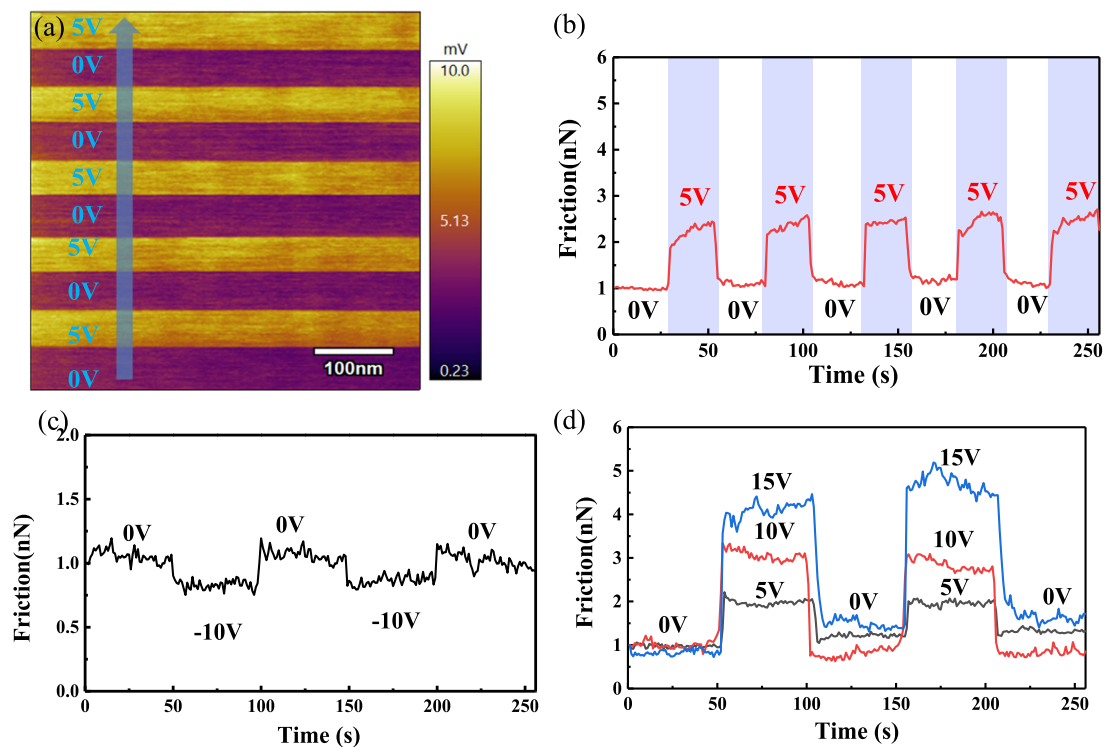


Fig. 8 Nanofriction modulation on atomically thin MoS₂. **a** Mapping of the nanofriction on atomically thin MoS₂ modulated dynamically under different V_g . Scale bar: 100 nm. **b** Corresponding profiles of the nanofriction indicated by the blue arrow line. **c** The nanofriction on atomically thin MoS₂ modulated by applying the negative V_g . **d** The nanofriction on atomically thin MoS₂ modulated by applying different positive V_g (the load for friction test was 10 nN).

friction under the positive gate voltage. Considering phononic friction is a constant, the electronic friction to the relative contribution of the two components increases with the increase of gate voltage.

The nanofriction induced phonons in atomically thin MoS₂ interact strongly with electrons due to EPC resulting in a new channel for energy dissipation of friction. The nanofriction on atomically thin MoS₂ increases with the increase of the carrier concentration, indicating that the energy dissipation of friction is consistent with the strengthening of EPC. The background carrier concentration was reduced by applying the negative V_g . Therefore, the decreased carrier concentration depresses the strength of the EPC to decrease the additional energy dissipation efficiency in atomically thin MoS₂. Then, the nanofriction on atomically thin MoS₂ correlates strongly with the carrier concentration. Therefore, active controlling of nanofriction on atomically thin MoS₂ could be obtained by tuning the carrier concentration based on gate voltage modulation.

Figure 8a shows 500 × 500 nm² frictional map (grayscale: bright, high nanofriction; dark, low nanofriction) on the atomically thin MoS₂ under the cyclic V_g of 5 V. The V_g was sequentially and dynamically modulated in the order of 0-5-0-5-0-5-0-5-0-5 V. A strip of nanofriction was observed from nanofriction map under the applied electric field. As shown in Fig. 8b, it is clearly observed that the nanofriction increases as the increase of V_g . Also, the changes of nanofriction on atomically thin MoS₂ are rapid and reversible during the switch of the V_g . Figure 8c shows the frictional profiles during the dynamic tuning of V_g between -10 V and 0 V. The nanofriction is reduced reversibly at $V_g = -10$ V and the nanofriction can also be fully recovered when the V_g return to 0 V, as shown in Fig. 8c. Figure 8d shows that the nanofriction is controlled stably and reversibly at high V_g , proving the high reliability of this nanofriction-tuning method. Figure 8d also shows that the nanofriction response has good repeatability and stability to the variation of V_g . The nanofriction can reduce by about 20% under the negative V_g (Fig. 8c) and increase about five times under the positive V_g (Fig. 8d). In particular, the effect of the negative and positive V_g on the nanofriction have a significant difference. Therefore, actively tuning of nanofriction on atomically thin MoS₂ in a dynamic, reversible, and controllable way is achieved based on the field effect modulation of the carrier.

In summary, the electronic friction and energy dissipation on atomically thin MoS₂ were investigated using calibrated AFM under different V_g . The electronic friction and energy dissipation on atomically thin MoS₂ correspond strongly with the V_g modulated strength of EPC. The linear fitting of electronic friction and carrier concentration of atomically thin MoS₂ was obtained by varying the strength of EPC with controllable carrier concentrations. The friction on atomically thin MoS₂ can be tuned dynamically, repeatably, and controllably by gate-induced regulation of the carrier concentration. The electronic friction and energy dissipation of atomically thin MoS₂ based on EPC provides a novel method to control friction and provide the possibility for recent emerging applications of superlubricity. The electronic friction could extend the potential application of atomically thin 2D with semiconductors in various MEMS/NEMS to achieve intelligent friction.

METHODS

Fabrication of the atomically thin MoS₂ and AFM probe calibration

The natural MoS₂ bulk crystals used in this study are provided by SPI Supplies Inc. The atomically thin MoS₂ was prepared by mechanical exfoliation and then transferred to the p-doped Si substrate with a 300 nm thick SiO₂ insulation layer. The Si probes (Multi75Al-G, 3.0 N/m, Budget Sensors) with rectangular cantilevers were used for the nanofriction and topography measurements. The conductive probes with PtIr coating (EFM, Nano World Inc.) were used for surface potential measurements. The normal and lateral forces were calibrated using a noncontact method⁵⁹.

Topography, friction, and adhesion measurements

The topography and thickness of atomically thin MoS₂ were determined by AFM in tapping mode (MFP-3D, Asylum Research Inc). The nanofriction and adhesion measurements were accomplished on atomically thin MoS₂ using AFM in contact mode in an ambient environment (temperature ~22 °C, relative humidity ~30%). The nanofriction on atomically thin MoS₂ was measured in the scanning area of 500 × 500 nm² at the scanning speed of 1.25 μm/s. The adhesions were evaluated by the pull-off force from force-distance measurements with a Si probe. Adhesion force was measured five times to take the average value. The SiO₂/Si substrate was placed on the conductive gold foil for the connection of the external electric field. The positive and negative values of the gate voltages (V_g) were applied to the conductive gold foil during the nanofriction and adhesion measurements.

Surface potential measurements

The surface potential of atomically thin MoS₂ was measured by scanning Kelvin force microscopy (SKPM) under an ambient condition with different gate voltages. The spring constant and resonance frequency of the conductive probe for surface potential measurements was 2.8 N/m and 75 kHz, respectively.

Raman spectroscopy characterization of atomically thin MoS₂

Room-temperature Raman spectra were recorded with 532-nm line of an argon ion laser as exciting radiation with a Witec confocal spectrometer using a 50 × long working distance objective. Laser power was kept below 1 mW to avoid heating samples. The positive and negative gate voltages were also applied to the conductive gold foil on the SiO₂/Si substrate during Raman measurements.

DATA AVAILABILITY

The data that support the plots within this paper and other findings of this study are available from the corresponding author upon reasonable request.

Received: 23 September 2021; Accepted: 16 May 2022;

Published online: 09 June 2022

REFERENCES

1. Chu, S. & Majumdar, A. Opportunities and challenges for a sustainable energy future. *Nature* **488**, 294–303 (2012).
2. Holmberg, K. & Erdemir, A. Influence of tribology on global energy consumption. *Costs Emiss. Frict.* **5**, 263–284 (2017).
3. Carpick, R. W. Controlling friction. *Science* **313**, 184–185 (2006).
4. Socoliuc, A. et al. Atomic-scale control of friction by actuation of nanometer-sized contacts. *Science* **313**, 207–210 (2006).
5. He, F. et al. In-plane potential gradient induces low frictional energy dissipation during the stick-slip sliding on the surfaces of 2D materials. *Small* **15**, 1904613 (2019).
6. Feng, X. et al. Superlubric sliding of graphene nanosheets on graphene. *ACS Nano* **7**, 1718–1724 (2013).
7. Li, H. et al. Superlubricity between MoS₂ Monolayers. *Adv. Mater.* **29**, 1701474 (2017).
8. Spear, J. C., Ewers, B. W. & Batteas, J. D. 2D-nanomaterials for controlling friction and wear at interfaces. *Nano Today* **10**, 301–314 (2015).
9. Szlufarska, I., Chandross, M. & Carpick, R. W. Recent advances in single-asperity nanotribology. *J. Phys. D. Appl. Phys.* **41**, 123001 (2008).
10. Andersson, D. & de Wijn, A. S. Understanding the friction of atomically thin layered materials. *Nat. Commun.* **11**, 420 (2020).
11. Fajardo, O. Y. & Mazo, J. J. Surface defects and temperature on atomic friction. *J. Phys. Condens. Mat.* **23**, 355008 (2011).
12. Filletter, T. et al. Friction and dissipation in epitaxial graphene films. *Phys. Rev. Lett.* **102**, 086102 (2009).
13. Lee, H. et al. Isotope- and thickness-dependent friction of water layers intercalated between graphene and mica. *Tribol. Lett.* **66**, 36 (2018).
14. Quereda, J., Castellanos-Gomez, A., Agraiet, N. & Rubio-Bollinger, G. Single-layer MoS₂ roughness and sliding friction quenching by interaction with atomically flat substrates. *Appl. Phys. Lett.* **105**, 053111 (2014).
15. Peng, Y. et al. Nanotribological characterization of graphene on soft elastic substrate. *Carbon* **124**, 541–546 (2017).

16. Lee, C. et al. Frictional characteristics of atomically thin sheets. *Science* **328**, 76–80 (2010).
17. Li, S. Z. et al. The evolving quality of frictional contact with graphene. *Nature* **539**, 541–546 (2016).
18. Zhang, S. A. et al. Tuning friction to a superlubric state via in-plane straining. *P. Natl Acad. Sci. USA* **117**, 6951–6951 (2019).
19. Li, Q. Y. et al. Fluorination of graphene enhances friction due to increased corrugation. *Nano Lett.* **14**, 5212–5217 (2014).
20. Sun, X. Y., Wu, R. N., Xia, R., Chu, X. H. & Xu, Y. J. Effects of stone-wales and vacancy defects in atomic-scale friction on defective graphite. *Appl. Phys. Lett.* **104**, 2605 (2014).
21. Lang, H. J., Peng, Y. T., Shao, G. W., Zou, K. & Tao, G. M. Dual control of the nanofriction of graphene. *J. Mater. Chem. C* **7**, 6041–6051 (2019).
22. Zeng, X. Z., Peng, Y. T. & Lang, H. J. A novel approach to decrease friction of graphene. *Carbon* **118**, 233–240 (2017).
23. Zheng, X. H. et al. Robust ultra-low-friction state of graphene via Moiré superlattice confinement. *Nat. Commun.* **7**, 13204 (2016).
24. Wang, W., Dietzel, D. & Schirmeisen, A. Single-asperity sliding friction across the superconducting phase transition. *Sci. Adv.* **6**, eaay0165 (2020).
25. Dou, W. & Subotnik, J. E. Perspective: How to understand electronic friction. *J. Chem. Phys.* **148**, 230901 (2018).
26. Park, J. Y. & Salmeron, M. Fundamental aspects of energy dissipation in friction. *Chem. Rev.* **114**, 677–711 (2014).
27. Dong, Y. L. Effects of substrate roughness and electron-phonon coupling on thickness-dependent friction of graphene. *J. Phys. D: Appl. Phys.* **47**, 055305 (2014).
28. Park, J. Y., Ogletree, D. F., Thiel, P. A. & Salmeron, M. Electronic control of friction in silicon pn junctions. *Science* **313**, 186–186 (2006).
29. Yan, J., Zhang, Y. B., Kim, P. & Pinczuk, A. Electric field effect tuning of electron-phonon coupling in graphene. *Phys. Rev. Lett.* **98**, 166802 (2007).
30. Park, J. Y., Qi, Y., Ogletree, D. F., Thiel, P. A. & Salmeron, M. Influence of carrier density on the friction properties of Silicon pn junctions. *Phys. Rev. B* **76**, 064108 (2007).
31. Ahn, C. H. et al. Electrostatic modification of novel materials. *Rev. Mod. Phys.* **78**, 1185–1212 (2006).
32. Ling, X. et al. Raman enhancement effect on two-dimensional layered materials: graphene, h-BN and MoS₂. *Nano Lett.* **14**, 3033 (2014).
33. Wang, Q. H., Kalantar-Zadeh, K., Kis, A., Coleman, J. N. & Strano, M. S. Electronics and optoelectronics of two-dimensional transition metal dichalcogenides. *Nat. Nanotechnol.* **7**, 699–712 (2012).
34. Ye, J. T. et al. Superconducting dome in a gate-tuned band insulator. *Science* **338**, 1193–1196 (2012).
35. Sarkar, D. et al. MoS₂ field-effect transistor for next generation label-free bio-sensors. *ACS Nano* **8**, 3992–4003 (2014).
36. Melitz, W., Shen, J., Kummel, A. C. & Lee, S. Kelvin probe force microscopy and its application. *Surf. Sci. Rep.* **66**, 1–27 (2011).
37. Koren, E., Rosenwaks, Y., Allen, J. E., Hemesath, E. R. & Lauhon, L. J. Nonuniform doping distribution along silicon nanowires measured by Kelvin probe force microscopy and scanning photocurrent microscopy. *Appl. Phys. Lett.* **95**, 092105 (2009).
38. Chakraborty, B. et al. Symmetry-dependent phonon renormalization in monolayer MoS₂ transistor. *Phys. Rev. B* **85**, 161403 (2012).
39. Socoliuc, A., Bennewitz, R., Gneco, E. & Meyer, E. Transition from stick-slip to continuous sliding in atomic friction: entering a new regime of ultralow friction. *Phys. Rev. Lett.* **92**, 134301 (2004).
40. Carpick, R. W., Ogletree, D. F. & Salmeron, M. Lateral stiffness: a new nano-mechanical measurement for the determination of shear strengths with friction force microscopy. *Appl. Phys. Lett.* **70**, 1548–1550 (1997).
41. Medyanik, S. N., Liu, W. K., Sung, I. H. & Carpick, R. W. Predictions and observations of multiple slip modes in atomic-scale friction. *Phys. Rev. Lett.* **97**, 136106 (2006).
42. Dagan, R. et al. Two-dimensional charge carrier distribution in MoS₂ monolayer and multilayers. *Appl. Phys. Lett.* **114**, 101602 (2019).
43. Maragliano, C. et al. Quantifying charge carrier concentration in ZnO thin films by scanning Kelvin probe microscopy. *Sci. Rep.* **4**, 4203 (2014).
44. Yu, Z. H. et al. Towards intrinsic charge transport in monolayer molybdenum disulfide by defect and interface engineering. *Nat. Commun.* **5**, 5290 (2014).
45. Li, Y. et al. Work function modulation of bilayer MoS₂ nanoflake by backgate electric field effect. *Appl. Phys. Lett.* **103**, 033122 (2013).
46. Lee, S. Y. et al. Large work function modulation of monolayer MoS₂ by ambient gases. *ACS Nano* **10**, 6100–6107 (2016).
47. Ellison, D. J. et al. Surface potential mapping of SAM-functionalized organic semiconductors by Kelvin probe force microscopy. *Adv. Mater.* **23**, 502–507 (2011).
48. Wang, Y., Udyavara, S., Neurock, M. & Frisbie, C. D. Field effect modulation of electrocatalytic hydrogen evolution at back-gated Two-Dimensional MoS₂ Electrodes. *Nano Lett.* **19**, 6118–6123 (2019).
49. Siao, M. D. et al. Two-dimensional electronic transport and surface electron accumulation in MoS₂. *Nat. Commun.* **9**, 1442 (2018).
50. Dagan, R., Vaknin, Y. & Rosenwaks, Y. Gap state distribution and Fermi level pinning in monolayer to multilayer MoS₂ field effect transistors. *Nanoscale* **12**, 8883–8889 (2020).
51. Rao, R., Yadav, R. A., Padma, N., Jagannath & Arvind, A. Investigation of electron-phonon interaction in bulk and nanoflakes of MoS₂ using anomalous "b" mode in the resonant Raman spectra. *J. Appl. Phys.* **128**, 165703 (2020).
52. Tamm, A. et al. Langevin dynamics with spatial correlations as a model for electron-phonon coupling. *Phys. Rev. Lett.* **120**, 185501 (2018).
53. Head-Gordon, M. & Tully, J. C. Molecular dynamics with electronic frictions. *J. Chem. Phys.* **103**, 10137–10145 (1995).
54. Lin, Z., Zhigilei, L. V. & Celli, V. Electron-phonon coupling and electron heat capacity of metals under conditions of strong electron-phonon nonequilibrium. *Phys. Rev. B* **77**, 430–446 (2008).
55. Weber, N. A. et al. Polaronic contributions to friction in a manganite thin film. *Adv. Sci.* **8**, 2003524 (2020).
56. Lang, H. J. et al. Atomic scale atomic-scale friction characteristics of graphene under conductive AFM with applied voltages. *ACS Appl. Mater. Inter.* **12**, 25503–25511 (2020).
57. Popov, V. L. & Gray, J. A. T. Prandtl–Tomlinson model: history and applications in friction, plasticity, and nanotechnologies. *Z. Angew. Math. Mech.* **92**, 683–708 (2012).
58. Song, A. S. et al. Fluctuation of interfacial electronic properties induces friction tuning under an electric field. *Nano Lett.* **22**, 1889–1896 (2022).
59. Wagner, K., Cheng, P. & Vezenov, D. Noncontact method for calibration of lateral forces in scanning force microscopy. *Langmuir* **27**, 4635–4644 (2011).

ACKNOWLEDGEMENTS

This work is supported by the National Natural Science Foundation of China (Grant Nos. 52075093, 51775105), the Fundamental Research Funds for the Central Universities, and the DHU Distinguished Young Professor Program.

AUTHOR CONTRIBUTIONS

B.S. performed the experiments, analyzed the data, and wrote the manuscript. Y.P. and X.G. analyzed the data and provided suggestions on the experimental design. K.Y., H.L., X.C. and K.Z. provided suggestions on the experimental design and manuscript writing. All authors discussed the results and revised the manuscript.

COMPETING INTERESTS

The authors declare no competing interests.

ADDITIONAL INFORMATION

Supplementary information The online version contains supplementary material available at <https://doi.org/10.1038/s41699-022-00316-6>.

Correspondence and requests for materials should be addressed to Yitian Peng.

Reprints and permission information is available at <http://www.nature.com/reprints>

Publisher's note Springer Nature remains neutral with regard to jurisdictional claims in published maps and institutional affiliations.



Open Access This article is licensed under a Creative Commons Attribution 4.0 International License, which permits use, sharing, adaptation, distribution and reproduction in any medium or format, as long as you give appropriate credit to the original author(s) and the source, provide a link to the Creative Commons license, and indicate if changes were made. The images or other third party material in this article are included in the article's Creative Commons license, unless indicated otherwise in a credit line to the material. If material is not included in the article's Creative Commons license and your intended use is not permitted by statutory regulation or exceeds the permitted use, you will need to obtain permission directly from the copyright holder. To view a copy of this license, visit <http://creativecommons.org/licenses/by/4.0/>.

© The Author(s) 2022